



Interfacial CoAl_2O_4 from ZIF-67@ $\gamma\text{-Al}_2\text{O}_3$ pellets toward catalytic activation of peroxymonosulfate for metronidazole removal

Min-Ping Zhu^{a,b}, Jia-Cheng E. Yang^{a,*}, Xiaoguang Duan^c, Dan-Dan Zhang^d, Shaobin Wang^c, Baoling Yuan^e, Ming-Lai Fu^{a,*}

^a Key Laboratory of Urban Pollutant Conversion, Institute of Urban Environment (IUE), Chinese Academy of Sciences (CAS), No. 1799, Jimei Avenue, Xiamen 361021, China

^b University of Chinese Academy of Sciences (UCAS), No. 19A, Yuquan Road, Shijingshan District, Beijing 100049, China

^c School of Chemical Engineering and Advanced Materials, The University of Adelaide, Adelaide, SA 5005, Australia

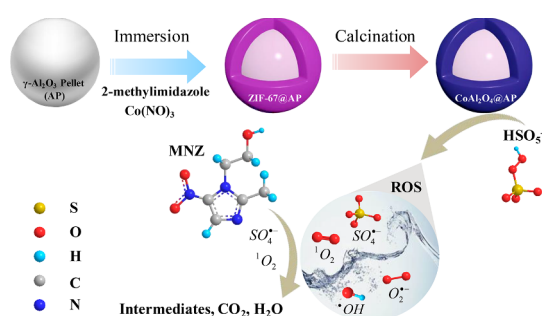
^d Key Lab of Urban Environment and Health, Institute of Urban Environment (IUE), Chinese Academy of Sciences (CAS), No. 1799, Jimei Avenue, Xiamen 361021, China

^e College of Civil Engineering Huaqiao University, Xiamen 361020, China

HIGHLIGHTS

- ZIF-67 derived CoAl_2O_4 @ $\gamma\text{-Al}_2\text{O}_3$ pellet (CoAl_2O_4 @AP) was synthesized.
- $\text{SO}_4^{\cdot-}$, $\cdot\text{OH}$, $^1\text{O}_2$ and $\text{O}_2^{\cdot-}$ were produced in the CoAl_2O_4 @AP/PMS system.
- $\text{SO}_4^{\cdot-}$ and $^1\text{O}_2$ played the vital roles in oxidative removal of metronidazole.
- CoAl_2O_4 @AP showed high activity, stability and reusability in catalytic reactions.

GRAPHICAL ABSTRACT



ARTICLE INFO

Keywords:

CoAl_2O_4
MOF
Peroxymonosulfate
Sulfate radical
Oxygen vacancy

ABSTRACT

Metal organic frameworks (MOFs)-based catalysts are rising stars in advanced oxidation processes (AOPs) to generate reactive oxygen species (ROS). Nevertheless, constructing an affordable and recyclable MOFs-derived catalyst with high reactivity and stability is highly desirable but still challenging. Herein, we unprecedentedly designed a novel CoAl_2O_4 @ $\gamma\text{-Al}_2\text{O}_3$ pellet (CoAl_2O_4 @AP) as a heterogeneous catalyst to activate peroxymonosulfate (PMS) toward ROS generation for metronidazole (MNZ) removal. A CoAl_2O_4 shell was formed on the pellet surface by direct calcination of the surface-nucleated ZIF-67 on $\gamma\text{-Al}_2\text{O}_3$ pellets. The strong and unique interactions between the Co species of ZIF-67 and $\gamma\text{-Al}_2\text{O}_3$ resulted in the formation of interfacial CoAl_2O_4 . The CoAl_2O_4 @AP exhibited a remarkably higher efficacy for PMS activation than ZIF-67-derived Co_3O_4 and commercial Co_3O_4 . The effects of several reaction parameters (i.e., PMS dosage, reaction temperature, initial pH, and background inorganic ions) on MNZ removal were comprehensively investigated and the degradation pathways of MNZ were elucidated. The $\text{Co}^{2+}/\text{Co}^{3+}$ and oxygen vacancies of CoAl_2O_4 @AP were the intrinsic active centers for PMS activation to simultaneously generate a diversity of ROS, among which $\text{SO}_4^{\cdot-}$ and $^1\text{O}_2$ played the decisive roles in MNZ decomposition. After the reaction, CoAl_2O_4 @AP can be easily separated from the bulk solution and regenerated via a PMS-assisted cleaning process, making the composites highly appealing for practical applications. This pioneering work on constructing microscopic CoAl_2O_4 -based composites expands the application of MOFs-based catalysts in novel AOPs systems for the treatment of persistent emerging pollutants.

* Corresponding authors.

E-mail addresses: jcyang@iue.ac.cn (J.-C.E. Yang), mlfu@iue.ac.cn (M.-L. Fu).

<https://doi.org/10.1016/j.cej.2020.125339>

Received 28 February 2020; Received in revised form 29 April 2020; Accepted 3 May 2020

Available online 05 May 2020

1385-8947/ © 2020 Elsevier B.V. All rights reserved.

1. Introduction

Despite the tremendous benefits of various antibiotics for treating human and animal infections, the persistence of the antibiotics in the environment has intensified, in particular, in aquatic ecosystems [1,2] due to the discharge of wastewater. Significant correlations between the antibiotic resistance and risks of human health have been previously reported [3–5]. It is therefore urgent to minimize the spread of antibiotics via controlling their discharge and release from human activities. Toward this goal, emerging technologies of advanced oxidation processes (AOPs) have been developed based on a wide array of peroxides such as hydrogen peroxide, ozone, and persulfates [6–12]. Reactive oxygen species (ROS), such as sulfate radical ($\text{SO}_4^{\cdot-}$) and hydroxyl radical ($\cdot\text{OH}$), can be produced by activating peroxymonosulfate (PMS) or peroxydisulfate (PDS) via thermal, ultrasound and ultraviolet stimulations [13–15], whereas these approaches require a high energy input. Transition metals, especially Co^{2+} , can effectively activate PMS to generate $\text{SO}_4^{\cdot-}$ [16,17]. However, the AOPs systems relying on homogeneous catalysis are restricted by the inherent drawbacks of secondary pollution and the difficulty in recycling the metal ions. Therefore, heterogeneous catalysts stand out as the substitutes to activate PMS to generate ROS without excessive addition of metal ions and the associated secondary contamination [8,18–24].

Up to date, most of efforts have been devoted to designing Co-based nanoscale catalysts (CNCs) [25]. Among them, CNCs derived from Co-based metal organic frameworks (Co-MOFs), such as ZIF-67 [26], are outstanding candidates due to the unique characteristics of MOFs, including high specific surface areas, hierarchically porous structure and tunable chemical compositions. Unfortunately, the performance of Co-MOFs-derived CNCs is still plagued by the inevitable aggregation during the operation in AOPs, due to their inherent high surface energy at the nanoscale [27–30]. Furthermore, the utilization of Co-MOFs derived CNCs in large-scale operations usually requires high investments of intensive energy and effort in the recycling and regenerating procedures, which limit their practical applications. In this regard, immobilizing Co-MOFs on macroscale supports, such as activated carbon pellets [31], zeolite beads [32], nickel foam [33], resin [34] or polypropylene membrane [35] to form highly dispersed and recyclable CNCs exalted as a feasible strategy to overcome the aforementioned engineering limitations. Moreover, Co-MOFs can be used as precursors to derive novel Co-based oxides and composites (e.g. Co_3O_4 [20,36], CoFe_2O_4 [29,30]) with higher activity and better stability. For example, commercial Al_2O_3 ceramic membrane has been explored as a support to immobilize ZIF-67 derived Co_3O_4 for PMS reactions [37]. The resultant Co_3O_4 within the Al_2O_3 ceramic membrane filter was responsible for PMS activation to generate $\text{SO}_4^{\cdot-}$ and $\cdot\text{OH}$ for sulfamethoxazole removal, and the composite membrane filter could be regenerated by a PMS-assisted cleaning process. However, the relatively higher cost of Al_2O_3 ceramic membrane may hinder the scale-up applications of Co_3O_4 nanoparticle functionalized membrane. Therefore, it is highly desirable to synthesize Co-MOFs-derived CNCs with low cost, high reactivity, reusability and stability for PMS-based AOPs. Meanwhile, it is also inspiring to explore the possibility of converting Co-MOFs into other novel structures of CNCs.

Encouraged by our previously successful works on the fabrication of separable composites in environmental remediation [38–40], in this work, we used the commercially affordable activated alumina pellets ($\gamma\text{-Al}_2\text{O}_3$, 3–5 mm in diameter) and the ZIF-67 as the precursors to synthesize CNCs to address the engineering bottlenecks. $\gamma\text{-Al}_2\text{O}_3$ pellets are selected as the support because of their high mechanical strength and thermodynamic stability under rigorous conditions. As expected, the evolved CoAl_2O_4 shells were successfully coated onto the surface of $\gamma\text{-Al}_2\text{O}_3$ pellets. The macroscopic $\text{CoAl}_2\text{O}_4@ \gamma\text{-Al}_2\text{O}_3$ pellet ($\text{CoAl}_2\text{O}_4@ \text{AP}$) was then used as a heterogeneous catalyst to activate PMS for degrading metronidazole (MNZ). MNZ was selected as a representative contaminant due to its ubiquitous occurrence in

wastewater at a mg/L level and potential risks to induce antibiotic resistance in waterborne bacteria [1,41]. To the best of our knowledge, this is the first study using CoAl_2O_4 -containing pellets as the catalysts for PMS activation. The advantages of using $\text{CoAl}_2\text{O}_4@ \text{AP}$ in AOPs lie in their low cost, scalable production, high activity and satisfactory reusability, which are of vital significance to extend their service life especially in practical fixed-bed operations.

2. Materials and methods

2.1. Materials

Some chemicals, 2-methylimidazole (2-MIM), Oxone ($\text{KHSO}_5 \cdot 0.5\text{KHSO}_4 \cdot 0.5\text{K}_2\text{SO}_4$) (as a PMS precursor), commercial nano- Co_3O_4 and metronidazole (MNZ) were supplied by Aladdin, China. Cobalt (II) nitrate hexahydrate ($\text{Co}(\text{NO}_3)_2 \cdot 6\text{H}_2\text{O}$), methanol, ethanol (EtOH), *tert*-butanol (TBA), *p*-benzoquinone (BQ), γ -histidine (HD), sodium hydroxide (NaOH), and nitric acid (HNO_3) were purchased from Sinopharm, Shanghai, China. All the chemicals, unless otherwise stated, were used without further purification. Commercial $\gamma\text{-Al}_2\text{O}_3$ pellets (APs, Sinopharm, Shanghai) with 3–5 mm in diameter were firstly washed using deionized (DI) water and then dried overnight at 105 °C prior to further usage.

2.2. Synthesis of $\text{CoAl}_2\text{O}_4@ \text{AP}$

The precursor of $\text{CoAl}_2\text{O}_4@ \text{AP}$, ZIF-67 modified AP (ZIF-67@AP), was synthesized by an *in-situ* growth method [37]. Firstly, APs were fully immersed into Solution A (480 mM of 2-MIM in methanol) for 30 min without stirring. This step was followed by methanol washing for three times. Subsequently, the resultant APs were placed into Solution B (60 mM of $\text{Co}(\text{NO}_3)_2 \cdot 6\text{H}_2\text{O}$ in methanol) for another 30 min without stirring. After washing with methanol, the samples were immediately transferred into the mixtures of Solution A and B without disturbance. After aging for 24 h, the purple products were separated and washed with methanol and DI water for several times, and dried at 105 °C overnight to obtain ZIF-67@AP. The as-obtained ZIF-67@AP was calcined under 450 °C for 3 h in static air with a heating rate of 5 °C/min. After cooling to room temperature naturally, the blue products were obtained, washed by DI water and dried at 105 °C overnight, denoted as $\text{CoAl}_2\text{O}_4@ \text{APs}$. For comparison, ZIF-67 powders were prepared according to the reported methods [37], and the obtained ZIF-67 powders were subject to calcination at 450 °C for 3 h to synthesize ZIF-67 derived Co_3O_4 nanoparticles.

2.3. Characterizations

The surface morphologies as well as elemental distributions were acquired by a field emission scanning electron microscope (FESEM, S-4800, Hitachi, Japan) coupling with energy dispersive X-ray spectroscopy (EDX). X-ray diffraction (XRD) spectra of samples were recorded on an X'Pert PRO diffractometer (PANalytical, Holland, Cu K_α , $\lambda = 0.15406$ nm) with 40 kV accelerating voltage and 40 mA current. The wide-angle data were collected from 5° to 80° at a scan speed of 0.6°/min. UV–Vis absorption spectra were detected on a spectrophotometer (UV3600, Shimadzu, Japan) with an integrating sphere and BaSO_4 was used as the reference sample. Meanwhile, X-ray photoelectron spectroscopy (XPS) analysis was used to determine the surface elemental compositions and valence states of $\text{CoAl}_2\text{O}_4@ \text{AP}$ related materials.

2.4. Evaluation of catalytic activity

Batch experiments were performed to assess the catalytic efficacy of $\text{CoAl}_2\text{O}_4@ \text{APs}$ for PMS activation. In each degradation reaction, a certain amount of catalysts ($\text{CoAl}_2\text{O}_4@ \text{APs}$) and 80 mL of MNZ (20 mg/

L) were separately transferred to 100 mL-flat conical flasks with ground-in glass stoppers. The bottles were then fixed on a temperature-controlled orbital shaker with a constant shaking rate of 300 rpm. After reaching the adsorption equilibrium between the catalysts and MNZ, a certain dose of PMS was added into the solution to initiate the reaction. At specific time intervals, 1 mL of the aqueous sample was withdrawn and quickly quenched with 0.25 mL of ethanol. The sample was filtered through a 0.22 μm cellulose acetate membrane for further concentration analysis. Three sets of control experiments were also conducted under the identical reaction conditions: i) experiments using ZIF-67@APs, ZIF-67 derived Co_3O_4 powders, or commercial nano- Co_3O_4 as the activators, ii) experiments without the addition of the catalyst or oxidant, and iii) homogeneous activation experiments by cobalt ions released from CoAl_2O_4 @APs (20 g/L) after activating PMS for 90 min. Unless otherwise specified, all the experiments were carried out in duplicate, and mean values and error bars were presented.

The concentrations of residual MNZ in solutions were analyzed using a high-performance liquid chromatography (HPLC) system (Agilent 1260, USA) equipped with a diode array detector and a

Poreshell 120 EC-C18 column (4.6×250 mm, $4 \mu\text{m}$, Agilent). The mobile phase was a mixture of 20/80 (v/v) acetonitrile–water with a flow rate of 1 mL/min at 30°C , and the detecting wavelength was 318 nm. A HPLC/mass spectrometry (MS)/MS system (Thermo Scientific Q Exactive Ultimate 3000 UPLC, USA) was used to detect the intermediates. The loading of Co ions on CoAl_2O_4 @APs and the leached concentrations of Co from CoAl_2O_4 @APs/PMS system were detected by inductively coupled plasma optical emission spectrometry (ICP-OES, Optima 7000DV, PerkinElmer, USA). The concentration of residual PMS in solution was analyzed by a UV–Vis spectrometer (Evolution 300, Thermo, USA) following the procedure developed by Liang et al. [42]. The total organic carbon (TOC) was measured by using a TOC analyzer (TOC-V CPH, Shimadzu, Japan) and aqueous $\text{Na}_2\text{S}_2\text{O}_3$ was used to quench the samples before TOC analysis. Additionally, *E. coli* K12 was used as a mode bacterial to study the potential biotoxicity of the by-products according to our previous work [43].

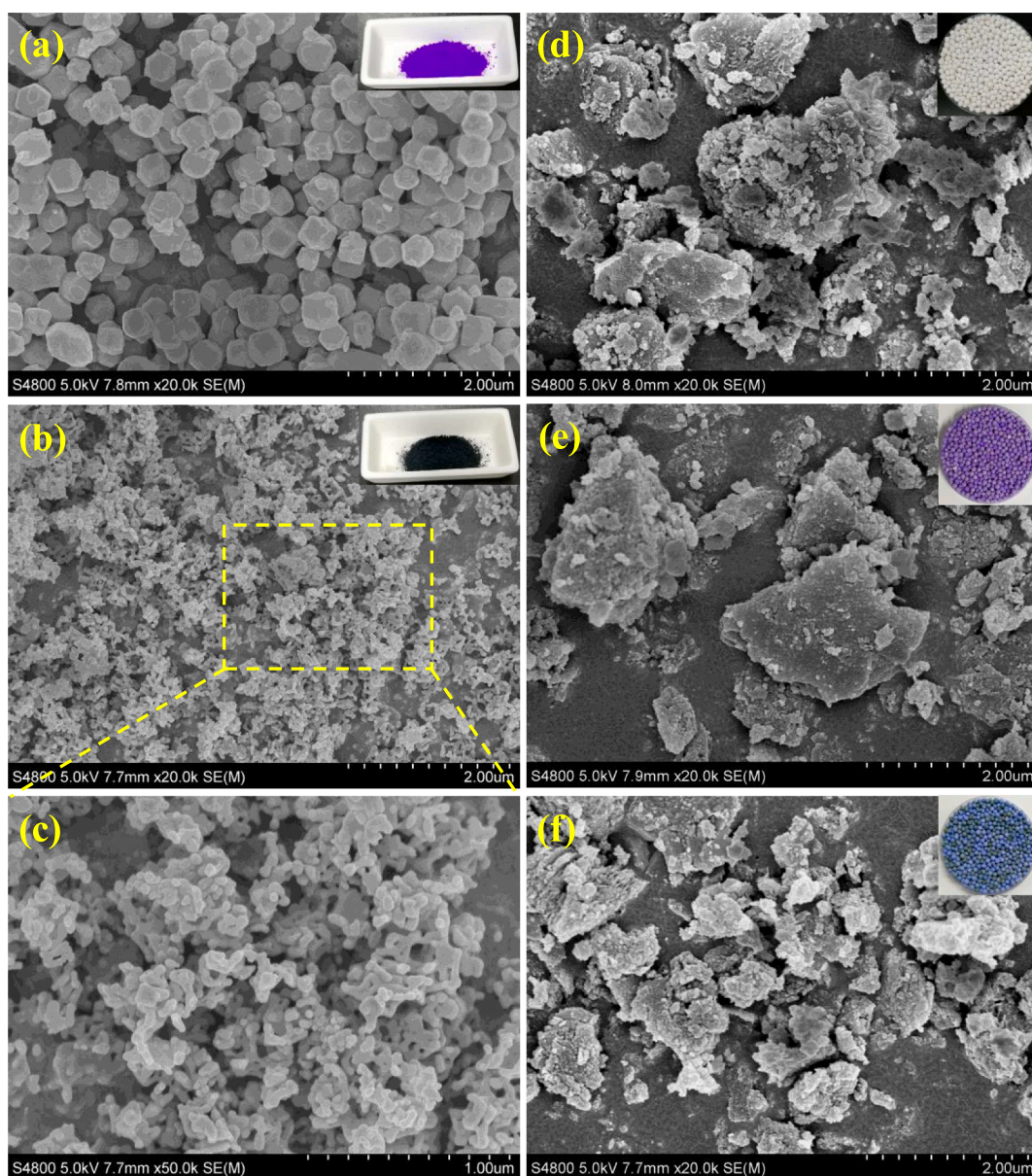


Fig. 1. SEM images of ZIF-67 (a), ZIF-67 derived Co_3O_4 (b and c), AP (d), ZIF-67@AP (e) and CoAl_2O_4 @AP (f). The inserts in SEM images are the optical pictures of ZIF-67, ZIF-67 derived Co_3O_4 , AP, ZIF-67@AP and CoAl_2O_4 @AP.

3. Results and discussion

3.1. Physicochemical characterizations

The morphologies of CoAl_2O_4 @APs samples are shown in Fig. 1. The bare ZIF-67 exhibits uniform and rhombic dodecahedron structures within with particle sizes range of 150–500 nm (Fig. 1a). After calcination at 450 °C for 3 h, the pristine polyhedral structures completely collapsed into nanosized grain-like aggregates with irregular morphologies (Fig. 1 b and c). Meanwhile, the color has also changed from bright purple (ZIF-67) to black (Co_3O_4). The particle sizes of ZIF-67 derived Co_3O_4 are in the range of 40–100 nm (Fig. 1c). Large blocks with rough surface are found for CoAl_2O_4 @AP-related samples (Fig. 1d-f). The in-situ formation of ZIF-67 and subsequent calcination did not change the pristine morphologies of AP samples despite that the color was changed from white to purple, and finally to blue. Noting that the color of CoAl_2O_4 @AP surface is not black as an Al_2O_3 ceramic membrane immobilized Co_3O_4 catalyst derived from ZIF-67 [37], which is probably due to the different surface property of supports.

XRD measurements were conducted to study the crystallographic structures of ZIF-67@AP derived samples (Fig. 2). Three distinguishable peaks at around 37.6°, 45.8° and 67.0° were detected for all the samples, which are the typical diffraction peaks of the [3 1 1], [4 0 0] and [4 4 0] planes for $\gamma\text{-Al}_2\text{O}_3$ (JCPDS#: 10-0425), respectively. The additional peaks at 14.5°, 28.2°, and 72.0° were also observed for AP, indicating the existence of boehmite ($\text{Al}(\text{OH})_3$) (JCPDS#: 83-2384). Interestingly, several new peaks at 18.8°, 20.5° and 40.7° emerged for ZIF-67@AP, ascribed to the formation of bayerite ($\text{Al}(\text{OH})_3$) (JCPDS#: 74-1119). Therefore, in situ growth of ZIF-67 on AP surface would result in the hydration of $\gamma\text{-Al}_2\text{O}_3$ and change the surface structures of AP. When ZIF-67@APs were subject to pyrolysis, the characteristic peaks of $\text{Al}(\text{OH})_3$ and $\text{Al}(\text{OH})_3$ disappeared, due to the dehydration of $\text{Al}(\text{OH})_3$ and $\text{Al}(\text{OH})_3$ at high temperatures. After reacting with PMS, the characteristic peaks of $\text{Al}(\text{OH})_3$ appeared again, which was probably resulted from the hydration of the support surface in the aqueous environment. Unfortunately, we failed to detect the signals of Co-based oxides for ZIF-67@AP and CoAl_2O_4 @AP, despite that the characteristic peaks of Co_3O_4 were observed from the calcined ZIF-67 sample (Fig. S1). The energy dispersive X-ray (EDX) mapping implied the presence of cobalt in ZIF-67@AP and CoAl_2O_4 @AP, verifying the successful immobilization of Co onto the surface of AP (Fig. S2). The Al, O and C elements in the spectra originated from the pristine substrate and precursors used for the sample preparation.

UV-Vis spectroscopy in the region of 200–800 nm was used to further verify the cobalt species and the coordination chemistry of cobalt elements on AP surface. As depicted in Fig. 3, there are no peaks in AP assigned to Co-related oxides. When APs were in situ modified with ZIF-67, four absorption bands located at 540, 564, 582 and 620 nm emerged for the ZIF-67@AP samples. The former three peaks can be assigned to ${}^4\text{A}_2(\text{F}) \rightarrow {}^4\text{T}_1(\text{P})$ transition of tetrahedral Co^{2+} coordination, which is consistent with the previously identified Co^{2+} in ZIF-67 [44]. Additionally, the last peak at 620 nm matches well with the absorption band of $\alpha\text{-Co}(\text{OH})_2$, which also features a tetrahedral Co^{2+} site [45]. The formation of $\alpha\text{-Co}(\text{OH})_2$ could be ascribed to the coordination of surface Co with H_2O during the synthesis [46]. These findings imply the formation of ZIF-67 on AP. After calcination, the spectra of CoAl_2O_4 @AP show an intense triplet at 545, 580, and 630 nm, indicating the tetrahedrally coordinated Co^{2+} in the CoAl_2O_4 phase [47,48]. The blue color is owing to the absorption of light during the range of 545–630 nm. The Co species, i.e. CoAl_2O_4 , is barely reduced and formed during the migration of Co^{2+} into tetrahedral sites of the $\gamma\text{-Al}_2\text{O}_3$ lattice [49], which is of great advantage to defend the shedding of Co-based catalysts. Furthermore, another intense band centered at around 250 nm is also discernible in CoAl_2O_4 @AP sample, ascribed to electron transfer from O_2^{2-} to Co^{3+} in the octahedral coordination, giving rise to a distinct greenish hue to the samples [50,51]. The partial

oxidation of Co^{2+} to Co^{3+} was probably due to the gradient of Co concentration and the excessive Co^{2+} over CoAl_2O_4 @AP [49,52]. Interestingly, the UV-Vis absorption bands of the used CoAl_2O_4 @AP samples are similar to those of fresh CoAl_2O_4 @AP samples, suggesting the structural robustness of the CoAl_2O_4 @AP. Noting that no peaks at 380 nm and 700 nm were observed, indicating the absence of Co_3O_4 phase in ZIF-67@AP and CoAl_2O_4 @AP samples [47].

The chemical compositions and bonding configurations of ZIF-67@AP and CoAl_2O_4 @AP were investigated via XPS characterization and the C 1s peak at 284.8 eV was used as the reference. Fig. S3 depicts the peaks of Co 2p, O 1s, C 1s, and Al 2p for ZIF-67@AP and CoAl_2O_4 @AP, which are in good agreement with the observation of EDX characterization (Fig. S2). The Co $2\text{p}_{3/2}$ spectra of ZIF-67@AP manifest three peaks at 780.5, 782.1 and 786.1 eV (Fig. 4a) as found in ZIF-67 [46]. The first two peaks are the characteristic Co^{2+} species while the last peak is assigned to the shake-up satellite (marked as "Sat.") of Co^{2+} species, which are consistent with the UV-Vis results of ZIF-67 derived composites. Meanwhile, ZIF-67@AP shows another peak at 779.7 eV, assigned to Co^{3+} species, which is probably originated from the unstable $\alpha\text{-Co}(\text{OH})_2$ as analyzed by UV-Vis that were partially converted into $\text{CoO}(\text{OH})$ species [46]. After calcination at 450 °C, the Co $2\text{p}_{3/2}$ spectra of CoAl_2O_4 @AP (Fig. 4b) also consist of two Co species. Specifically, the peak at 779.7 eV confirms the existence of Co^{3+} , whereas those at 780.9 and 782.3 eV belong to the high-spin Co^{2+} species [53,54]. The board peak at 786.4 eV is a typical shake-up satellite of high-spin Co^{2+} species [55,56], which stems from the distributions of Co^{2+} in tetrahedral and octahedral sites [57]. Clearly, the binding energy of Co^{2+} species in CoAl_2O_4 @AP is slightly higher than that of ZIF-67@AP by 0.4, 0.2, and 0.3 eV, respectively. Such peak shifting, on the basis of UV-Vis results, might be attributed to the gradual phase transition from Co-OH of ZIF-67 to $\alpha\text{-Co}(\text{OH})_2$, and ultimately CoAl_2O_4 . It should be noted that the area ratio of $\text{Co}^{2+}/\text{Co}^{3+}$ for CoAl_2O_4 @AP is 6.81, while the ratio for ZIF-67@AP is only 3.87, suggesting that the density of oxygen vacancy of CoAl_2O_4 @AP is higher than that of ZIF-67@AP [58]. Meanwhile, the O 1s spectra of ZIF-67@AP and CoAl_2O_4 @AP can be deconvoluted into three components [36], including lattice oxygen species (529.9 eV, marked as $\text{O}_{\text{Lattice}}$), oxygen defects (531.1 eV, marked as O_{Defect}), and hydroxyl groups or surface-adsorbed oxygen species (532.1 eV, marked as $\text{O}_{\text{Surface}}$). The higher $\text{O}_{\text{Defect}}/\text{O}_{\text{Lattice}}$ ratio of CoAl_2O_4 @AP also indicates that the CoAl_2O_4 @AP (6.89)

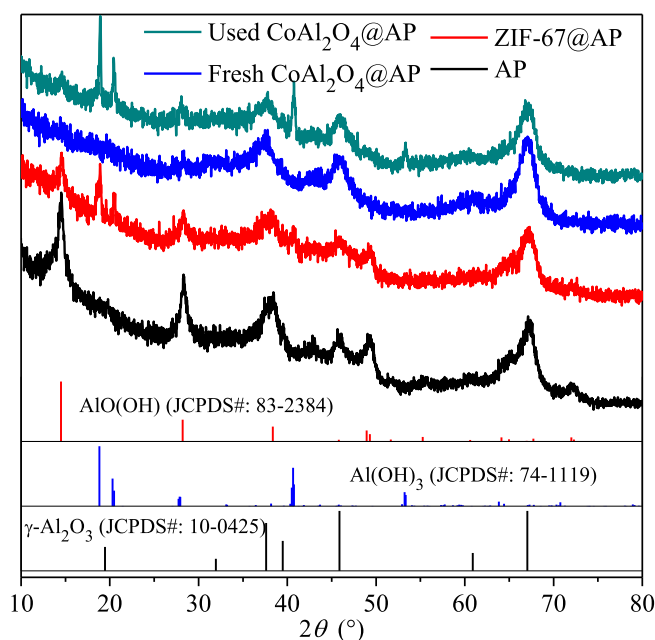


Fig. 2. XRD spectra of AP, ZIF-67@AP and CoAl_2O_4 @AP.

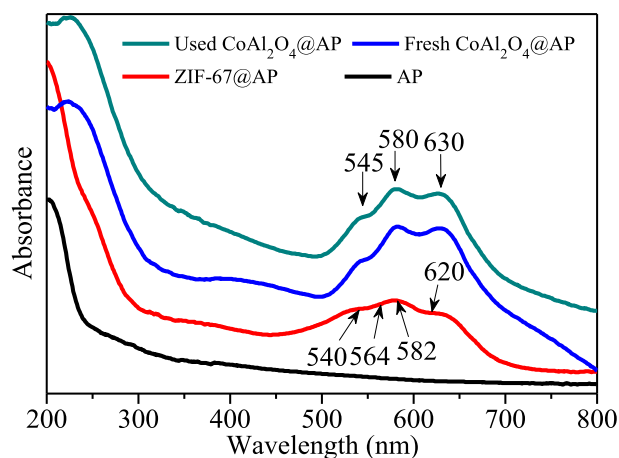


Fig. 3. UV-Vis spectra of AP, ZIF-67@AP and CoAl_2O_4 @AP.

possessed more oxygen vacancies than ZIF-67@AP (0.85), which might be helpful to improving the catalytic activity of the CoAl_2O_4 @AP towards PMS activation.

3.2. Catalytic performance

Fig. 5 shows the comparison of MNZ removal efficiencies over CoAl_2O_4 @AP and other catalysts including ZIF-67@AP, commercial nano- Co_3O_4 powders and ZIF-67 derived Co_3O_4 powders. Four control experiments were conducted including MNZ alone, MNZ oxidation by sole PMS, adsorption removal by sole CoAl_2O_4 @AP, and homogeneous Co^{2+} /PMS systems. Less than 4% of MNZ was removed by sole PMS, implying that self-decomposition of PMS could not generate sufficient ROS for MNZ removal. Meanwhile, an extremely low MNZ removal efficiency (1%) was obtained by CoAl_2O_4 @AP alone, revealing that the CoAl_2O_4 @AP had almost no adsorption capacity toward MNZ. Besides, the contribution of MNZ removal by natural volatilization was very limited and could be ignored.

In the catalytic systems, 33%, 67% and 5% of MNZ concentrations were reduced by PMS activated with ZIF-67@AP (20 g/L), ZIF-67 derived Co_3O_4 (4 g/L), and commercial nano- Co_3O_4 (4 g/L), respectively.

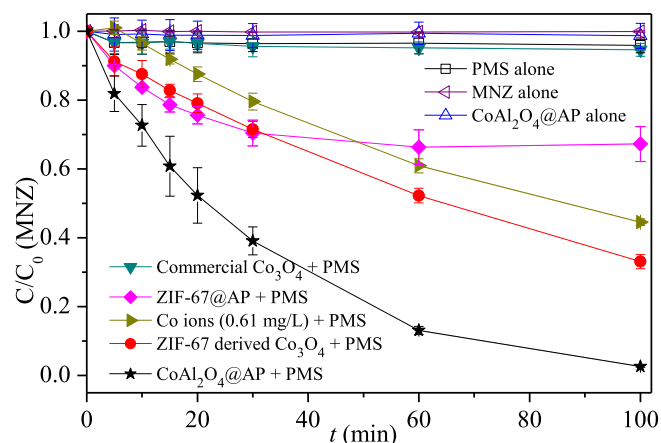


Fig. 5. MNZ removal by PMS activated with different materials ($[\text{PMS}]_0 = 1.0 \text{ mM}$, $[\text{CoAl}_2\text{O}_4\text{@AP}] = [\text{ZIF-67@AP}] = 20 \text{ g/L}$, $[\text{Co}_3\text{O}_4] = 4 \text{ g/L}$, $[\text{MNZ}]_0 = 20 \text{ mg/L}$, $\text{pH} = 6.48$, $T = 25 \pm 1 \text{ }^\circ\text{C}$).

Encouragingly, MNZ removal was markedly enhanced and reached 97% within 100 min when CoAl_2O_4 @AP (20 g/L) was used as an activator. In the current study, the Co loading amount on CoAl_2O_4 @AP was around 0.30 wt% (detected by ICP-OES), implying that the maximal dosage of CoAl_2O_4 participated in PMS activation was 180 mg/L, which is much lower than Co_3O_4 powders (4 g/L). These results implied that CoAl_2O_4 @AP is a highly effective catalyst to activate PMS for ROS generation and MNZ decomposition, due to the well-dispersed and highly reactive CoAl_2O_4 layer formed on the macro-sized AP supports. In addition, only trace Co ions (0.61 mg/L) were leached from the CoAl_2O_4 @AP/PMS system, and the contrasted removal efficiency of MNZ by homogeneous Co/PMS system was 55% within 100 min. Obviously, PMS was heterogeneously activated by the CoAl_2O_4 @AP composite rather than the leached Co ions.

3.3. Reaction parameters-regulated MNZ removal

3.3.1. Effect of PMS dosage

As revealed in Fig. 6a, MNZ removal was enhanced with the increased dosage of PMS. Specifically, when 0.5 mM of PMS was used,

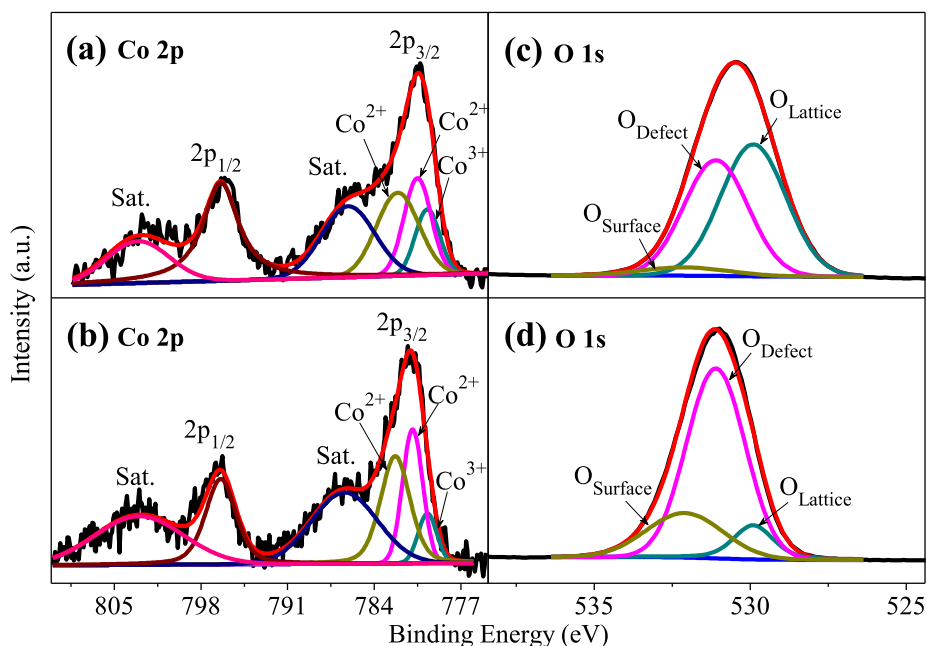


Fig. 4. XPS analysis for Co 2p and O 1s of ZIF-67@AP (a, c) and CoAl_2O_4 @AP (b, d).

only ~40% of MNZ was removed in 60 min, suggesting that PMS was insufficient in this system. A dramatic enhancement in MNZ removal was obtained by increasing the PMS dosage to 1.0 mM. The removal efficiency at the PMS dosage of 1 mM was two times higher than that of 0.5 mM, and the first-order reaction rate constants (k_{obs}) for MNZ removal remarkably increased from 0.014 to 0.032 min^{-1} . Further increasing PMS dosage from 1 to 3 mM linearly augmented the k_{obs} values (Fig. 6b), ascribed to the fact that increasing PMS dosage would produce more ROS to speed up the MNZ oxidation.

3.3.2. Effect of solution temperature

Fig. 7 shows that the MNZ removal was boosted with the elevated solution temperature from 15 to 35 °C. For example, a complete MNZ removal was achieved within 30 min at 35 °C, while only 36% of MNZ was removed at 15 °C within the same period. By fitting the kinetic model, MNZ removal was found to follow the first-order reaction kinetics and their rate constants were 0.014, 0.032 and 0.18 min^{-1} at 15, 25 and 35 °C, respectively. As MNZ oxidation by $\text{CoAl}_2\text{O}_4\text{/PMS}$ is a surface catalytic process, the activation energy (E_a) could be calculated by the following Arrhenius-type equation:

$$\ln k_T = -E_a/RT + \ln A$$

where k_T is the first-order reaction rate constant (min^{-1}) at different temperatures (T , K); E_a is the activation energy for degradation (kJ/mol); A is a time pre-factor while R is the gas constant of 8.314 J/(K·mol). By fitting k_T versus $-1/T$, E_a was calculated to be 41.32 kJ/mol, suggesting that MNZ removal by $\text{CoAl}_2\text{O}_4\text{/PMS}$ was a chemical reaction-limited process.

3.3.3. Effect of initial solution pH

The effect of initial solution pH (3.23–10.86) on MNZ removal was investigated (Fig. 8). The pH induced PMS self-decomposition toward MNZ removal was very limited at the initial pH range from 3.23 to 9.08. At higher initial pH 10.86, only about 22% of MNZ was removed, which was due to the alkaline activation of PMS [59]. $\text{CoAl}_2\text{O}_4\text{/PMS}$ coupled system exhibited a higher MNZ removal efficiency than bare PMS oxidation system over initial pH 3.23–10.86, verifying the positive role of $\text{CoAl}_2\text{O}_4\text{/PMS}$ in PMS activation/catalysis. The pH-regulated performance of $\text{CoAl}_2\text{O}_4\text{/PMS}$ is probably ascribed to the electrostatic interactions of $\text{CoAl}_2\text{O}_4\text{/AP}$, MNZ and/or PMS for producing ROS [60]. In the current study, pH_{PZC} of $\text{CoAl}_2\text{O}_4\text{/AP}$ was determined to be 7.9. The pK_{a2} value of PMS is 9.4 [61], while the pK_a value of MNZ is 2.6 [62]. The solution pH after reaction generally increased with the increased initial pH (Table S1). In the case of initial pH < 9.08, $\text{CoAl}_2\text{O}_4\text{/AP}$ was mainly positively charged, and the PMS molecules presented in the form of HSO_5^- . At this stage, the electrostatic attraction between $\text{CoAl}_2\text{O}_4\text{/AP}$ and HSO_5^- is favorable for activating HSO_5^- into ROS. In this context, $\text{CoAl}_2\text{O}_4\text{/AP/PMS}$ can maintain high MNZ removal. At initial pH 10.86, the transformation of HSO_5^- to SO_5^{2-} was expected, while $\text{CoAl}_2\text{O}_4\text{/AP}$ was negatively charged. The

electrostatic repulsion of SO_5^{2-} and $\text{CoAl}_2\text{O}_4\text{/AP}$ gave rise to a deleterious effect on the decomposition of PMS and the formation of ROS.

3.3.4. Effect of co-existing inorganic anions

As shown in Fig. 9, the presence of different inorganic anions (i.e., NO_3^- , PO_4^{3-} , HCO_3^- , SO_4^{2-} , and Cl^-) caused varying effects on MNZ removals. With respect to the removal efficiency in 100 min, 10 mM HCO_3^- and 10 mM Cl^- showed remarkable inhibitions on MNZ removal, while 10 mM PO_4^{3-} , 10 mM SO_4^{2-} and 10 mM NO_3^- exerted slight inhibition effects. In detail, < 20% of MNZ removal can be attained in the presence of HCO_3^- or Cl^- , while the removal efficiency can maintain at above 90% for PO_4^{3-} , SO_4^{2-} and NO_3^- . However, with respect to k_{obs} for MNZ removal, PO_4^{3-} exhibited a significant enhancement in MNZ removal and the k_{obs} value increased by 1.4 times compared with the control group, whereas for SO_4^{2-} and NO_3^- , the k_{obs} values decreased by 1.5 and 1.6 times, respectively. Compared to $\text{CoAl}_2\text{O}_4\text{/PMS}$ system without ions, the k_{obs} values for the cases of HCO_3^- and Cl^- decreased by 6.1 and 8.7 times, respectively. The positive influence of 10 mM PO_4^{3-} is probably ascribed to the fact that PMS could be pre-activated by the phosphate anions [63], which was favorable for the subsequent $\text{CoAl}_2\text{O}_4\text{/AP}$ catalysis. This is also partially confirmed by the current work, in which over 22% of MNZ was removed by a PO_4^{3-} (10 mM) /PMS system (without $\text{CoAl}_2\text{O}_4\text{/AP}$) in Fig. S4. The negative impact of SO_4^{2-} is a result of the formation of less reactive $\text{S}_2\text{O}_8^{2-}$ via Reaction 1 [64]. The inhibition effect of NO_3^- may be resulted from the scavenging reactions between NO_3^- and $\text{SO}_4^{\cdot-}$, and the subsequent formation of $\text{NO}_3^{\cdot-}$ with a lower oxidation potential Reaction 2 [64]. With respect to either the removal efficiency or the k_{obs} values, the inhibitory effect of HCO_3^- or Cl^- was much stronger than that of NO_3^- or SO_4^{2-} . Such a significant inhibition effect of Cl^- might be caused by the formation of less reactive chlorine species like HOCl (Reactions 3–5) [64] while the inhibitory effect of HCO_3^- was due to its reaction with $\text{SO}_4^{\cdot-}$ and $\cdot\text{OH}$, accompanying with the formation of much less reactive radical of $\text{CO}_3^{\cdot-}$ (Reactions 6 and 7) [65].

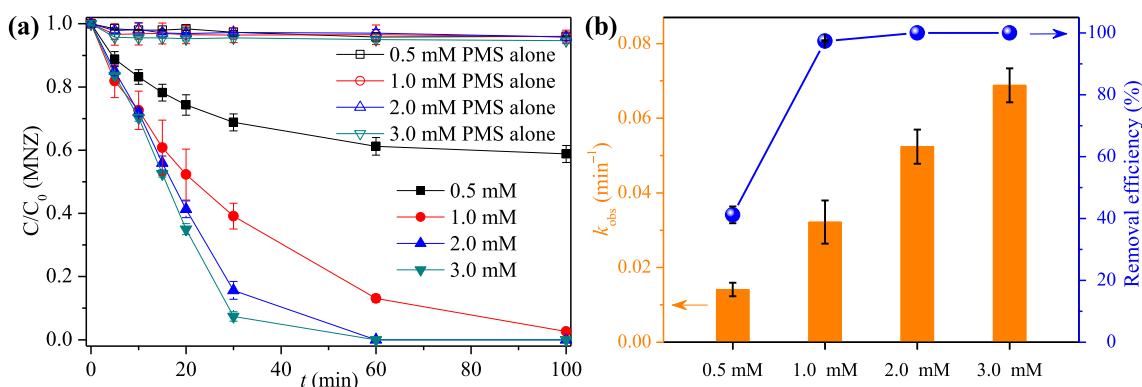
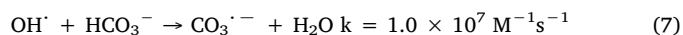
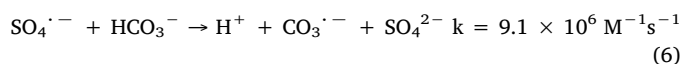
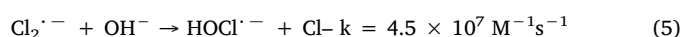
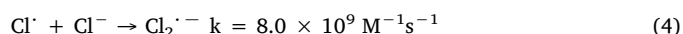
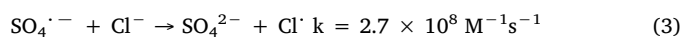
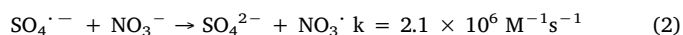
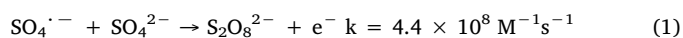


Fig. 6. Effect of PMS dosage on MNZ removal ($[\text{CoAl}_2\text{O}_4\text{/AP}] = 20 \text{ g/L}$, $[\text{MNZ}]_0 = 20 \text{ mg/L}$, $\text{pH} = 6.48$, $T = 25 \pm 1 \text{ }^\circ\text{C}$).

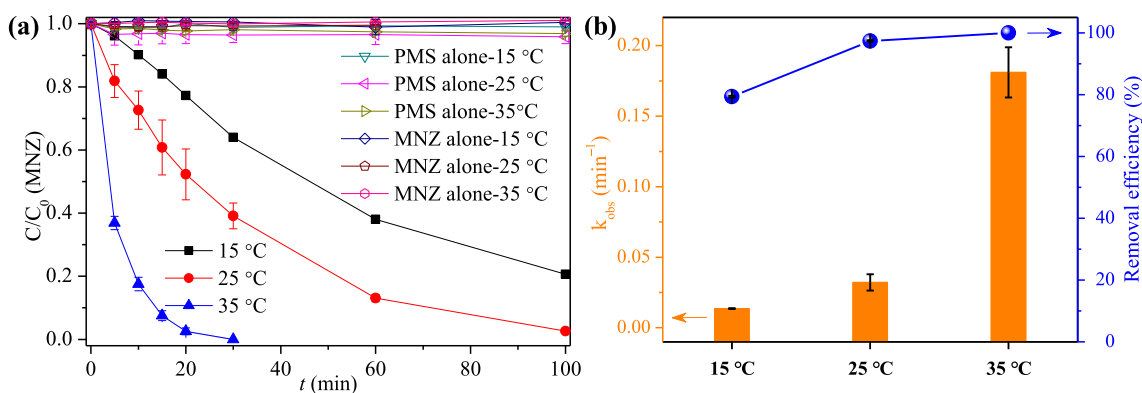


Fig. 7. Effect of solution temperature on MNZ removal ($[\text{CoAl}_2\text{O}_4@\text{AP}] = 20 \text{ g/L}$, $[\text{MNZ}]_0 = 20 \text{ mg/L}$, $[\text{PMS}]_0 = 1.0 \text{ mM}$, $\text{pH} = 6.48$).

3.4. Stability and recyclability of $\text{CoAl}_2\text{O}_4@\text{AP}$

The reusability and stability of $\text{CoAl}_2\text{O}_4@\text{AP}$ was assessed in multiple runs. The fresh $\text{CoAl}_2\text{O}_4@\text{AP}$ was firstly subject to activating PMS for MNZ removal. The used monolithic $\text{CoAl}_2\text{O}_4@\text{AP}$ was then harvested by a simple gauze-based filtration from bulk solution, followed by being washed with sufficient DI water and dried at 105 °C. The collected $\text{CoAl}_2\text{O}_4@\text{AP}$ was employed for a second run. The identical procedures were repeated for a third run of $\text{CoAl}_2\text{O}_4@\text{AP}$ toward PMS activation. The results in Fig. 10 indicated that a slight decrease (< 10%, from 97% to 92%) of MNZ removal efficiency was found for the second run. However, in the third run, the removal efficiency experienced a moderate decline (from 92% to 80%). The concentration of detected Co ions leached from $\text{CoAl}_2\text{O}_4@\text{AP}$ was 0.22 mg/L after the third run, which was still lower than the environmental quality standards for surface water of China (GB 3838–2002) (1 mg/L). PMS solution (1 mM) without MNZ was employed to treat the used $\text{CoAl}_2\text{O}_4@\text{AP}$, followed by washed with sufficient DI water and dried at 105 °C. After the cleaning with PMS solution, the catalytic efficacy of $\text{CoAl}_2\text{O}_4@\text{AP}$ was recovered with complete MNZ removal within 60 min in the fourth run. The decreased catalytic performance of $\text{CoAl}_2\text{O}_4@\text{AP}$ might be due to the presence of intermediates from oxidized MNZ, which covered the surface reactive sites of $\text{CoAl}_2\text{O}_4@\text{AP}$ and thus weakened their catalytic reactivity. Another reason might be the loss of active sites such as Co^{2+} species and defective O (refer to Reactions 8 and 9). The PMS-assisted cleaning process can not only eliminate the absorbed intermediates on $\text{CoAl}_2\text{O}_4@\text{AP}$ surface but also recover the active sites through a redox process (refer to Reactions 10 and 11). Obviously, $\text{CoAl}_2\text{O}_4@\text{AP}$ has an excellent catalytic activity and can be easily regenerated, which are attributed to the interfacial CoAl_2O_4 shell formed on micro-sized supports. These features indicate that $\text{CoAl}_2\text{O}_4@\text{AP}$ could be an attractive candidate for potential wastewater treatments because of their high performance and feasibility in

dead-end filtration processes or fixed-bed reactors.

3.5. Possible degradation mechanism

3.5.1. Interactions of $\text{CoAl}_2\text{O}_4@\text{AP}$ with PMS

In situ ATR-IR, confocal Raman and XPS characterizations were used to probe the PMS reaction with $\text{CoAl}_2\text{O}_4@\text{AP}$. The peaks found at 3272 ~ 3274 cm^{-1} in the ATR-IR spectra (Fig. 11a) are ascribed to the presence of hydrogen bonds between the surface adsorbed H_2O molecules on $\text{CoAl}_2\text{O}_4@\text{AP}$ and PMS. Over the activation course, the hydrogen bonds centered reactions achieved equilibrium, suggesting that such reactions were not responsible for PMS activation. Based on previous work [38], the peaks at around 1060, 1092 ~ 1101 and 1243 ~ 1244 cm^{-1} are due to the symmetric and/or asymmetric stretching vibrations of S–O bonds in PMS. A slight red shift (by 9 cm^{-1}) for the S–O bond from about 1101 to 1092 cm^{-1} was found when $\text{CoAl}_2\text{O}_4@\text{AP}$ were added into PMS solution for 30 min. The red shift implies that the electron density of S–O bond within HSO_5^- generally decreased because of the redox processes between HSO_5^- and active sites of $\text{CoAl}_2\text{O}_4@\text{AP}$. The surface catalytic centers of $\text{CoAl}_2\text{O}_4@\text{AP}$ interacted with the terminal H–O bond of HSO_5^- to withdraw electrons from the S–O bonds, thus elongating the S–O bond (neighboring H–O bond) and inducing a red shift. No shifts were detected when the reaction was prolonged to 80 min, indicating that the electron-donating/-withdrawing processes reached an equilibrium stage.

Three characteristic peaks from in situ confocal Raman spectra of PMS are shown in Fig. 11b. The peaks at around 882 cm^{-1} (marked as A), 981 cm^{-1} (marked as B) and 1062 cm^{-1} (marked as C) are due to the peroxide O–O bond, the stretching vibration modes of S–O bonds for SO_4^{2-} and HSO_5^- , respectively. The progressive decreases in intensities of A and C suggest the activation of PMS on $\text{CoAl}_2\text{O}_4@\text{AP}$. Obviously, both I_A/I_B and I_C/I_B values decreased with the proceeded reaction. The variation profiles indicated that the cleavages of peroxide

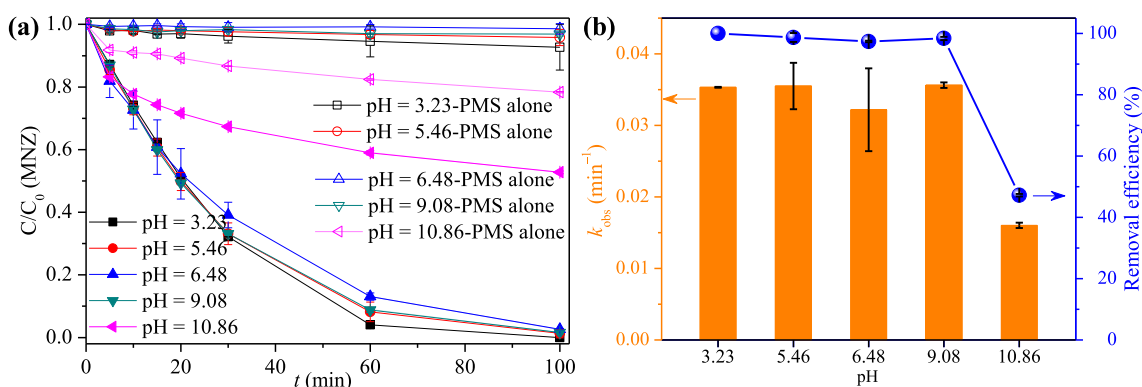


Fig. 8. Effect of initial pH values on MNZ removal ($[\text{CoAl}_2\text{O}_4@\text{AP}] = 20 \text{ g/L}$, $[\text{MNZ}]_0 = 20 \text{ mg/L}$, $[\text{PMS}]_0 = 1.0 \text{ mM}$, $T = 25 \pm 1 \text{ }^\circ\text{C}$).

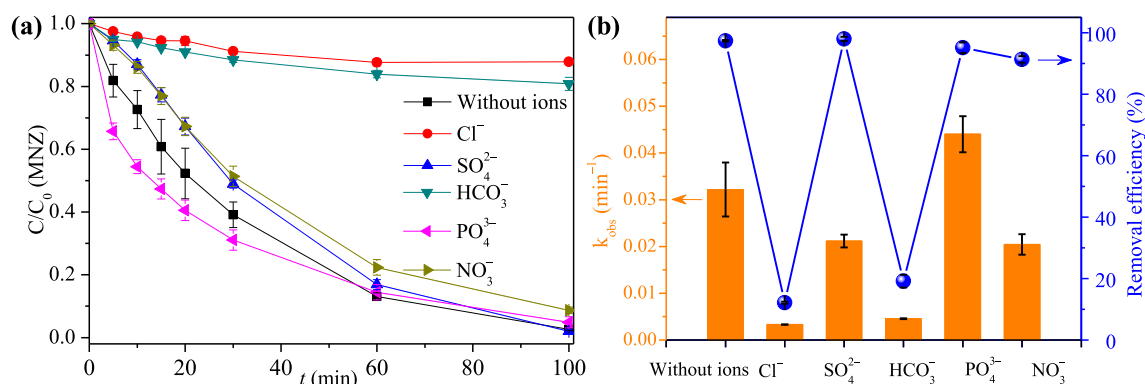


Fig. 9. Effect of co-existing inorganic ions on MNZ removal ($[CoAl_2O_4@AP] = 20$ g/L, $[MNZ]_0 = 20$ mg/L, $[PMS]_0 = 1.0$ mM, $[Cl^-] = [SO_4^{2-}] = [HCO_3^-] = [PO_4^{3-}] = [NO_3^-] = 10$ mM, pH = 6.48, T = 25 ± 1 °C).

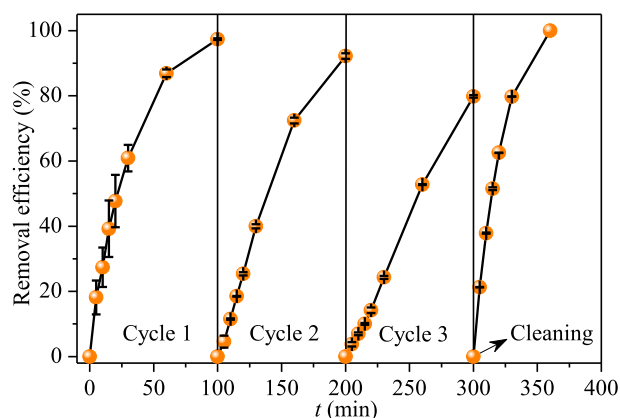


Fig. 10. Reusability of $CoAl_2O_4@AP$ toward PMS activation for MNZ removal ($[CoAl_2O_4@AP] = 20$ g/L, $[MNZ]_0 = 20$ mg/L, $[PMS]_0 = 1.0$ mM, pH = 6.48, T = 25 ± 1 °C).

bond and/or S–O bond occurred, giving rise to the formation of ROS.

The Co 2p and O 1s spectra of the used $CoAl_2O_4@AP$ are shown in Fig. 12. From the XPS fitting results (Figs. 4 and 12, Table 1), the oxidation states of surface Co and O elements had changed. For example, the contents of Co^{2+} and Co^{3+} changed from 52.88% and 7.77% for the fresh $CoAl_2O_4@AP$ to 48.91% and 20.03% for the used $CoAl_2O_4@AP$, respectively. The decreased ratio of Co^{2+}/Co^{3+} from 6.81 to 2.44 suggested the electron transfer from $CoAl_2O_4@AP$ to PMS, resulting in the formation of more Co^{3+} species because of the redox process of Co^{2+} species and PMS for ROS formation via Reactions 8 and 9 [15,53]. As show in Reactions 10 and 11 [17], more Co^{3+} species is favorable for the production of $SO_5^{\cdot-}$ (0.81 V_{NHE}) but detrimental to the formation of $\cdot OH$ (1.9–2.7 V_{NHE}) and $SO_4^{\cdot-}$ (2.6–3.1 V_{NHE}) [66,67], which explains the gradual decline of MNZ removal in the second and third run. After PMS-assisted cleaning, the activation efficacy of $CoAl_2O_4@AP$ was recovered in the fourth run, which probably resulted from the formation of Co^{2+} species mediated by the redox processes of Reactions 10 and 11. O 1s analysis (Figs. 4 and 12, Table 1) shows that, after the PMS reaction, the content of O_{Defect} and the ratio of $O_{Defect}/O_{Lattice}$ decreased, implying that the defects (such as oxygen vacancies) within $CoAl_2O_4@AP$ participated in PMS activation. The presence of oxygen vacancies is favorable for adsorbing PMS onto $CoAl_2O_4@AP$ surface, which undoubtedly facilitated PMS activation [68]. XPS analysis confirmed that the defects and electron-transfer reactions are critical for PMS activation by $CoAl_2O_4@AP$.

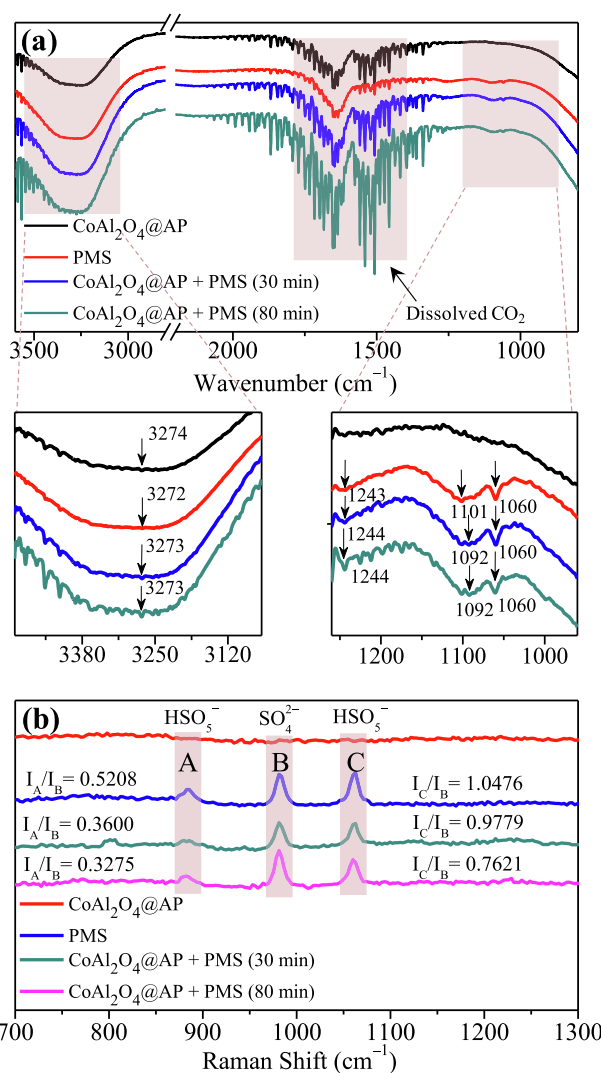
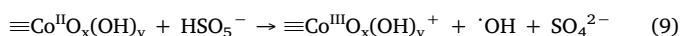
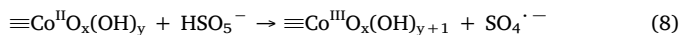
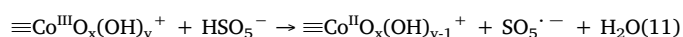
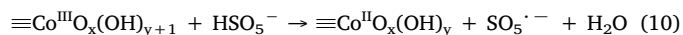


Fig. 11. In situ ATR-IR spectra (a) and Raman spectra (b) detected for $CoAl_2O_4@AP/PMS$ related reaction systems.



3.5.2. ROS in $CoAl_2O_4@AP/PMS$ system

Quenching experiments were carried out to probe the types of ROS

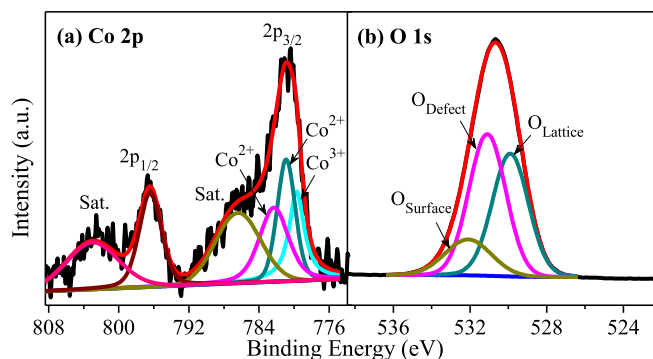


Fig. 12. XPS analysis for Co 2p (a) and O 1s (b) of used CoAl₂O₄@AP.

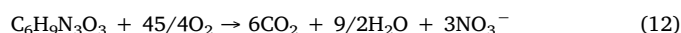
contributing to the MNZ oxidation in the CoAl₂O₄@AP/PMS system. Ethanol (EtOH) and *tert*-butanol (TBA) were first employed to determine the contributions of SO₄^{•-} and [•]OH. As shown in Fig. 13, 97% of MNZ was removed in 100 min without EtOH or TBA. When 5 mM EtOH was added into the reaction system, the removal efficiency of MNZ significantly decreased to ~39%. Further increasing the concentration of EtOH to 100 mM led to a complete inhibition to MNZ removal. However, TBA relatively weakly inhibited the MNZ removal. The removal efficiency can reach 80% with the addition of 100 mM TBA, much higher than that of the case with 5 mM EtOH. Even though the concentration of TBA increased to 500 mM, the removal efficiency was still higher than that of the system with 5 mM EtOH. Therefore, despite of the presence of [•]OH, SO₄^{•-} plays a decisive role in MNZ oxidation by the CoAl₂O₄@AP/PMS system. Other quenching agents, *p*-benzoquinone (BQ) and *L*-histidine (HD), were also employed to verify the roles of O₂^{•-} and ¹O₂ accordingly [69,70].

Previous work indicates that HD and BQ can directly consume PMS [38,70]. To verify this, we measured the decomposition of 1 mM PMS by 1 mM BQ and 1 mM HD. The results show that (Fig. S5), in current work, < 20% and 10% of PMS was decomposed for HD and BQ, respectively; however, complete decomposition of PMS by CoAl₂O₄@AP occurred. The *k*_{obs} value for PMS consumption was determined to be 0.031 min⁻¹, which was comparable to that for MNZ removal (0.032 min⁻¹) by CoAl₂O₄@AP activated PMS. These findings imply that HD or BQ induced PMS consumption was very limited. Therefore, 1 mM BQ and 1 mM HD were further used to probe the role of O₂^{•-} and ¹O₂ in MNZ removal. Fig. 13 shows that HD caused higher inhibition to MNZ removal than BQ, implying that ¹O₂ played a more important role than O₂^{•-}. This is because that, if the role of O₂^{•-} were stronger than ¹O₂, 1 mM BQ (1.2 × 10⁶ s⁻¹, 1 × 10⁵ s⁻¹, 3.8 × 10⁴ s⁻¹ and (0.9–1) × 10⁶ s⁻¹ for scavenging [•]OH, SO₄^{•-}, ¹O₂ and O₂^{•-}, respectively) would show much stronger inhibition to MNZ removal than 1 mM HD (5 × 10⁶ s⁻¹, 2.5 × 10⁶ s⁻¹, 6.6 × 10⁴ s⁻¹ and < 10⁻³ s⁻¹ for scavenging [•]OH, SO₄^{•-}, ¹O₂ and O₂^{•-}, respectively) [38]; however, the result is reverse. The inhibition effect of 100 mM EtOH (1.9 × 10⁸ s⁻¹, (1.6–7.8) × 10⁶ s⁻¹, 3.8 × 10² s⁻¹ and < 10² s⁻¹ for scavenging [•]OH, SO₄^{•-}, ¹O₂ and O₂^{•-}, respectively) is comparable to that for 1 mM HD, further verifying that both SO₄^{•-} and ¹O₂ are dominant ROS for MNZ removal. By comprehensively analyzing the quenching results, it is reasonable to infer that

multiple ROS (¹O₂, O₂^{•-}, SO₄^{•-} and [•]OH) were formed in CoAl₂O₄@AP/PMS system, and ¹O₂ and SO₄^{•-} were the decisive ROS in MNZ degradation [64].

3.5.3. MNZ mineralization and degradation products/pathways

TOC tests were employed to evaluate the MNZ mineralization by CoAl₂O₄@AP/PMS system. The result shows that the TOC removal efficiency increased with the increasing reaction time (Fig. S6). Typically, after 60 min reaction, the TOC removal efficiency reached 12.76%. When the reaction time increased to 100 min, the TOC removal efficiency increased to 18.83%. In theory, under a given volume, it will need 5.265 mM electrons from PMS to realize the complete degradation of 20 mg/L MNZ (refer to Reaction 12). Without interference, 1 mM PMS can provide 1 mM electrons. Following these rules, it can be concluded that about 18.99% of 20 mg/L MNZ can be mineralized, which is very close to the tested TOC removal efficiency (18.83%). The TOC removal efficiency after 100 min reaction is far lower than MNZ removal efficiency (97%), suggesting that most of MNZ molecules were probably transformed into other intermediates. Therefore, HPLC/MS/MS was used to probe the possible intermediates and oxidation pathways of MNZ by CoAl₂O₄@AP/PMS system.



Five kinds of by-products with *m/z* of 143.08, 117.07, 104.07, 172.07 and 202.08 were detected in the MS spectra with a positive ionization mode (Fig. S7). The relative distribution ratios for the products with *m/z* of 143.08, 117.07, 104.07, 172.07 and 202.08 are 11.12%, 14.90%, 4.15%, 57.68% and 12.14%, respectively. The negative ionization mode of HPLC/MS/MC is also used for product detection. However, there is no signal in this mode. This is attributed to the fact that MNZ is a compound containing -NO₂ group, which can be easily detected by the positive ionization mode of HPLC/MS/MS [71,72]. According to the *m/z* spectra, the tentative degradation products were proposed. Their molecular structures and *m/e* information are summarized in Fig. 14 and Table 2. In general, MNZ could be degraded by ROS through various pathways. In detail, direct oxidation of MNZ resulted in the formation of P₂₀₁-1, P₂₀₁-2 and P₂₀₁-3 (1–4). The resultant P₂₀₁-3 was further degraded to P₁₇₁-1 via decarboxylation/dehydrogenation processes (5) and to P₁₀₃-1/P₁₀₃-2 through the combined processes of decarboxylation, denitrification, chain cleavage, rearrangement and dehydration reactions (6–11). The pathways of 6–11 caused the formation of P₁₄₂-1, P₁₄₂-2, P₁₄₂-3 and P₁₄₂-4 (12–16). The combination of oxidation and decarboxylation led to the formation of P₁₇₁-2 (15, 17), and the direct denitrification process of P₁₇₁-1 and P₁₇₁-2 led to the formation of P₁₄₂-2 and P₁₄₂-5 (18, 19). The decarboxylation and oxidation further transformed P₁₄₂-4 and P₁₄₂-5 to P₁₁₆ (20, 21). As the oxidation proceeded, some of these by-products might eventually be mineralized into CO₂ and H₂O.

At last, the antibacterial activity experiments were conducted to study the biotoxicity of the by-products. However, the results showed that there is little change in bacterial population of *E. coli* K12 treated with DI water, 20 mg/L MNZ solution before and after reaction by CoAl₂O₄@AP/PMS system. This result implies that there exists no biotoxicity change for *E. coli* K12 (Fig. S8). We think this is probably due to the insensitivity of *E. coli* K12. The precise evaluation merits an

Table 1

XPS fitting results for the Co 2p and O 1s of ZIF-67@AP, fresh CoAl₂O₄@AP, and used CoAl₂O₄@AP.

Sample	Co 2p				O 1s			
	Co ²⁺	Co ³⁺	Satellite	Co ²⁺ /Co ³⁺	O _{Lattice}	O _{Defect}	O _{Surface}	O _{Defect} /O _{Lattice}
ZIF-67@AP	53.60	13.86	32.54	3.87	51.83	43.86	4.31	0.85
Fresh CoAl ₂ O ₄ @AP	52.88	7.77	39.35	6.81	10.01	68.95	21.04	6.89
Used CoAl ₂ O ₄ @AP	48.91	20.03	31.06	2.44	39.77	45.78	14.44	1.15

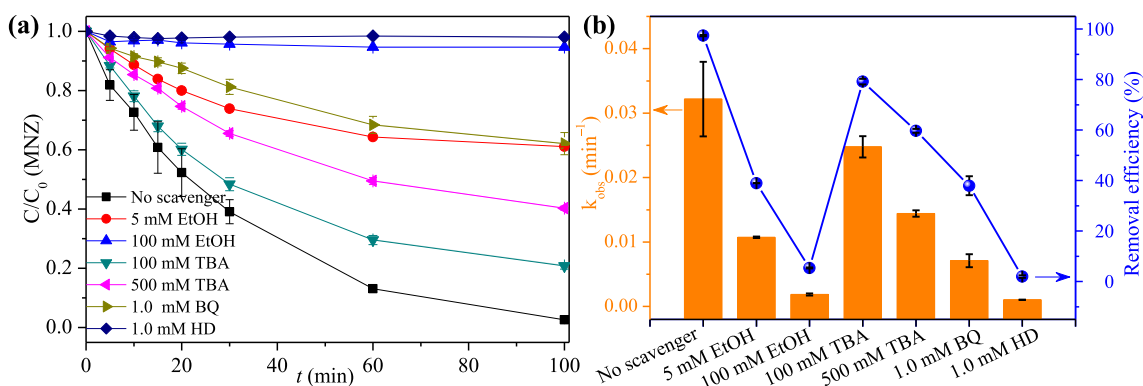


Fig. 13. Effect of various scavengers on MNZ removal ($[\text{CoAl}_2\text{O}_4@\text{AP}] = 20 \text{ g/L}$, $[\text{MNZ}]_0 = 20 \text{ mg/L}$, $[\text{PMS}]_0 = 1.0 \text{ mM}$, $\text{pH} = 6.48$, $T = 25 \pm 1 \text{ }^\circ\text{C}$).

in-depth study using sensitive bacterial, like *Vibrio fischeri*, as the testing organisms for the toxicity monitoring of by-products [73].

4. Conclusions

In this work, we successfully synthesized a interfacial CoAl_2O_4 shell/layer $\gamma\text{-Al}_2\text{O}_3$ pellet ($\text{CoAl}_2\text{O}_4@\text{AP}$) through a combined strategy of in situ growth of ZIF-67 onto the pellet surface and the subsequent calcination. The $\text{CoAl}_2\text{O}_4@\text{AP}$ composites demonstrated unprecedentedly catalytic activity to activate PMS toward ROS generation for MNZ removal. Benefitted from the unique coordination reactions of Co, Al and O elements, CoAl_2O_4 as the heterogeneous catalytic species within $\text{CoAl}_2\text{O}_4@\text{AP}$ exhibited a higher catalytic activity than ZIF-67 derived Co_3O_4 and commercial Co_3O_4 toward PMS activation. The

effects of PMS dosage, solution temperature, initial pH and co-existing ions on MNZ removal and the possible degradation pathways of MNZ were investigated. $\text{Co}^{2+}/\text{Co}^{3+}$ and oxygen vacancies within $\text{CoAl}_2\text{O}_4@\text{AP}$ facilitated the generation of $\text{SO}_4^{\cdot-}$, $\cdot\text{OH}$, $\text{O}_2^{\cdot-}$ and $^1\text{O}_2$ from the activated PMS. $\text{SO}_4^{\cdot-}$ and $^1\text{O}_2$ were identified as the decisive ROS in MNZ removal. The catalytic reactivity of aged $\text{CoAl}_2\text{O}_4@\text{AP}$ can be recovered via a PMS-assisted cleaning procedure, which holds a great promise in practical applications. This work provides new insights into constructing monolithic CoAl_2O_4 -containing catalysts toward ROS generation and expands the application of novel MOFs-based catalysts for environmental remediation.

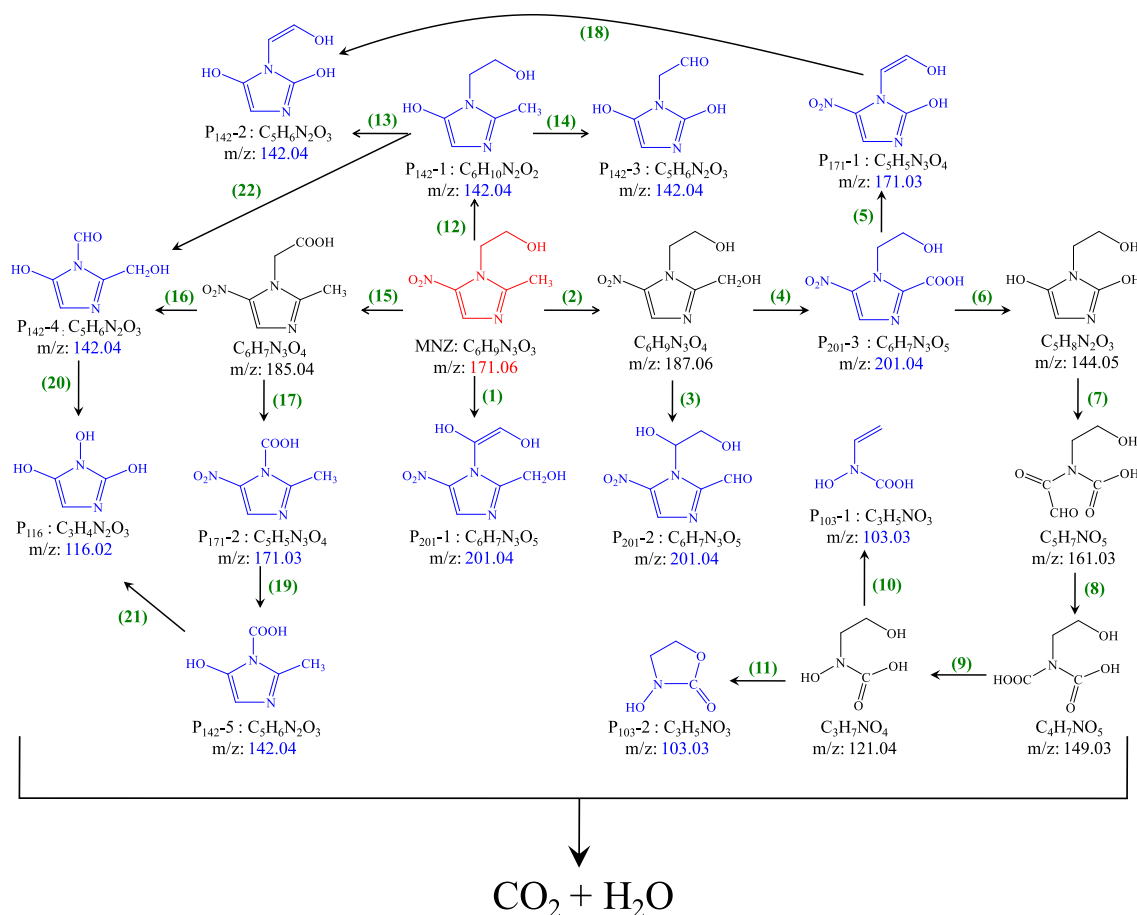


Fig. 14. Proposed oxidation products and pathways for MNZ degradation by $\text{CoAl}_2\text{O}_4@\text{AP}/\text{PMS}$ system.

Table 2
Intermediate products of MNZ during the treatment process detected by HPLC/MS/MS.

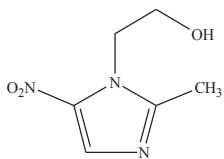
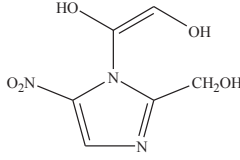
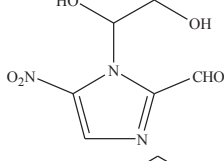
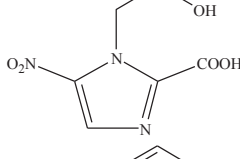
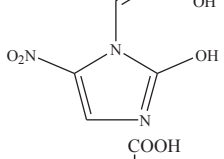
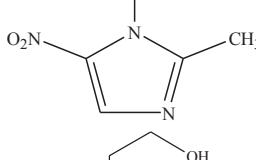
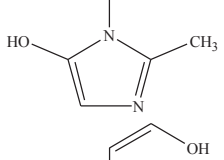
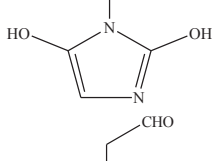
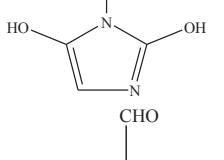
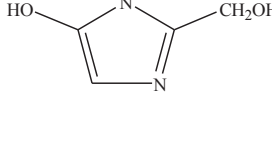
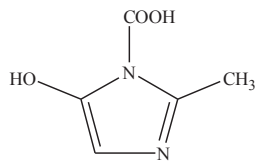
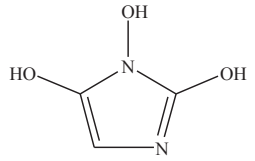
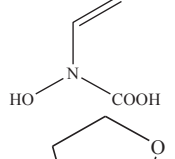
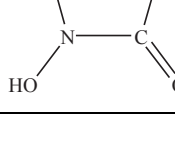
Item	Rt	MW	Molecular formula	Structural formula
MNZ	6.01	171.06	C ₆ H ₉ N ₃ O ₃	
P ₂₀₁₋₁	6.41	201.04	C ₆ H ₇ N ₃ O ₅	
P ₂₀₁₋₂	6.41	201.04	C ₆ H ₇ N ₃ O ₅	
P ₂₀₁₋₃	6.41	201.04	C ₆ H ₇ N ₃ O ₅	
P ₁₇₁₋₁	6.01	171.03	C ₅ H ₅ N ₃ O ₄	
P ₁₇₁₋₂	6.01	171.03	C ₅ H ₅ N ₃ O ₄	
P ₁₄₂₋₁	1.34	142.04	C ₆ H ₁₀ N ₂ O ₂	
P ₁₄₂₋₂	1.34	142.04	C ₅ H ₆ N ₂ O ₃	
P ₁₄₂₋₃	1.34	142.04	C ₅ H ₆ N ₂ O ₃	
P ₁₄₂₋₄	1.34	142.04	C ₅ H ₆ N ₂ O ₃	

Table 2 (continued)

Item	Rt	MW	Molecular formula	Structural formula
P ₁₄₂₋₅	1.34	142.04	C ₅ H ₆ N ₂ O ₃	
P ₁₁₆	1.69	116.02	C ₃ H ₄ N ₂ O ₃	
P ₁₀₃₋₁	1.99	103.03	C ₃ H ₅ NO ₃	
P ₁₀₃₋₂	1.99	103.03	C ₃ H ₅ NO ₃	

Declaration of Competing Interest

The authors declare that they have no known competing financial interests or personal relationships that could have appeared to influence the work reported in this paper.

Acknowledgment

We greatly appreciate the financial supports from National Natural Science Foundation of China (Grant Nos. 51778598, 51808524 and 51478449).

Appendix A. Supplementary data

Supplementary data to this article can be found online at <https://doi.org/10.1016/j.cej.2020.125339>.

References

- [1] I. Michael, L. Rizzo, C.S. McArdell, C.M. Manaia, C. Merlin, T. Schwartz, C. Dagot, D. Fatta-Kassinos, Urban wastewater treatment plants as hotspots for the release of antibiotics in the environment: A review, *Water Res.* 47 (2013) 957–995.
- [2] S. Zhang, B. Han, J. Gu, C. Wang, P. Wang, Y. Ma, J. Cao, Z. He, Fate of antibiotic resistant cultivable heterotrophic bacteria and antibiotic resistance genes in wastewater treatment processes, *Chemosphere* 135 (2015) 138–145.
- [3] D. Wu, Z. Huang, K. Yang, D. Graham, B. Xie, Relationships between antibiotics and antibiotic resistance gene levels in municipal solid waste leachates in Shanghai, China, *Environ. Sci. Technol.* 49 (2015) 4122–4128.
- [4] C.W. Knapp, J. Dolfing, P.A.I. Ehlert, D.W. Graham, Evidence of increasing antibiotic resistance gene abundances in archived soils since 1940, *Environ. Sci. Technol.* 44 (2010) 580–587.
- [5] A. Zarei-Baygi, M. Harb, P. Wang, L.B. Stadler, A.L. Smith, Evaluating antibiotic resistance gene correlations with antibiotic exposure conditions in anaerobic membrane bioreactors, *Environ. Sci. Technol.* 53 (2019) 3599–3609.
- [6] M. Pirsahab, H. Hossaini, H. Janjani, Reclamation of hospital secondary treatment effluent by sulfate radicals based-advanced oxidation processes (SR-AOPs) for removal of antibiotics, *Microchem. J.* 104430 (2019).
- [7] X. Li, B. Wu, Q. Zhang, D. Xu, Y. Liu, F. Ma, Q. Gu, F. Li, Mechanisms on the impacts of humic acids on persulfate/Fe²⁺-based groundwater remediation, *Chem. Eng. J.* 378 (2019) 122142.
- [8] J.C. Espinosa, P. Manickam-Periyaraman, F. Bernat-Quesada, S. Sivanesan, M. Álvaro, H. García, S. Navalón, Engineering of activated carbon surface to enhance the catalytic activity of supported cobalt oxide nanoparticles in peroxymonosulfate activation, *Appl. Catal. B Environ.* 249 (2019) 42–53.

- [9] J. Yan, J. Li, J. Peng, H. Zhang, Y. Zhang, B. Lai, Efficient degradation of sulfamethoxazole by the CuO@Al₂O₃ (EPC) coupled PMS system: Optimization, degradation pathways and toxicity evaluation, *Chem. Eng. J.* 359 (2019) 1097–1110.
- [10] Q. Yang, Y. Ma, F. Chen, F. Yao, J. Sun, S. Wang, K. Yi, L. Hou, X. Li, D. Wang, Recent advances in photo-activated sulfate radical-advanced oxidation process (SR-AOP) for refractory organic pollutants removal in water, *Chem. Eng. J.* 378 (2019) 122149.
- [11] Y. Wang, S. Hui, S. Zhan, R. Djellabi, J. Li, X. Zhao, Activation of peroxymonosulfate by novel Pt/Al₂O₃ membranes via a nonradical mechanism for efficient degradation of electron-rich aromatic pollutants, *Chem. Eng. J.* 381 (2020) 122563.
- [12] H. Milh, B. Schoenaers, A. Stesmans, D. Cabooter, R. Dewil, Degradation of sulfamethoxazole by heat-activated persulfate oxidation: Elucidation of the degradation mechanism and influence of process parameters, *Chem. Eng. J.* 379 (2020) 122234.
- [13] W. Oh, Z. Dong, T. Lim, Generation of sulfate radical through heterogeneous catalysis for organic contaminants removal: Current development, challenges and prospects, *Appl. Catal. B Environ.* 194 (2016) 169–201.
- [14] G. Boczkaj, A. Fernandes, Wastewater treatment by means of advanced oxidation processes at basic pH conditions: A review, *Chem. Eng. J.* 320 (2017) 608–633.
- [15] M. Gagol, A. Przyjazny, G. Boczkaj, Wastewater treatment by means of advanced oxidation processes based on cavitation – A review, *Chem. Eng. J.* 338 (2018) 599–627.
- [16] D. Zhou, L. Chen, J. Li, F. Wu, Transition metal catalyzed sulfite auto-oxidation systems for oxidative decontamination in waters: A state-of-the-art minireview, *Chem. Eng. J.* 346 (2018) 726–738.
- [17] G.P. Anipsitakis, D.D. Dionysiou, Degradation of organic contaminants in water with sulfate radicals generated by the conjunction of peroxymonosulfate with cobalt, *Environ. Sci. Technol.* 37 (2003) 4790–4797.
- [18] W. Du, Q. Zhang, Y. Shang, W. Wang, Q. Li, Q. Yue, B. Gao, X. Xu, Sulfate saturated biosorbent-derived Co-S@NC nanoarchitecture as an efficient catalyst for peroxymonosulfate activation, *Appl. Catal. B Environ.* 118302 (2019).
- [19] R. Zhang, Y. Wan, J. Peng, G. Yao, Y. Zhang, B. Lai, Efficient degradation of atrazine by LaCoO₃/Al₂O₃ catalyzed peroxymonosulfate: Performance, degradation intermediates and mechanism, *Chem. Eng. J.* 372 (2019) 796–808.
- [20] M. Abdul Nasir Khan, P. Kwame Klu, C. Wang, W. Zhang, R. Luo, M. Zhang, J. Qi, X. Sun, L. Wang, J. Li, Metal-organic framework-derived hollow Co₃O₄/carbon as efficient catalyst for peroxymonosulfate activation, *Chem. Eng. J.* 363 (2019) 234–246.
- [21] R. Yuan, Z. Jiang, Z. Wang, S. Gao, Z. Liu, M. Li, G. Boczkaj, Hierarchical MnO₂ nanoflowers blooming on 3D nickel foam: A novel micro-macro catalyst for peroxymonosulfate activation, *J. Colloid Interf. Sci.* 571 (2020) 142–154.
- [22] R. Yuan, M. Jiang, S. Gao, Z. Wang, H. Wang, G. Boczkaj, Z. Liu, J. Ma, Z. Li, 3D mesoporous α-Co(OH)₂ nanosheets electrodeposited on nickel foam: A new generation of macroscopic cobalt-based hybrid for peroxymonosulfate activation, *Chem. Eng. J.* 380 (2020) 122447.
- [23] R.D.C. Soltani, Z. Miraftebi, M. Mahmoudi, S. Jorfi, G. Boczkaj, A. Khataee, Stone cutting industry waste-supported zinc oxide nanostructures for ultrasonic assisted decomposition of an anti-inflammatory non-steroidal pharmaceutical compound, *Ultrason. Sonochem.* 58 (2019) 104669.
- [24] N.S. Shah, J.A. Khan, M. Sayed, Z.U.H. Khan, A.D. Rizwan, N. Muhammad, G. Boczkaj, B. Murtaza, M. Imran, H.M. Khan, G. Zaman, Solar light driven degradation of norfloxacin using as-synthesized Bi³⁺ and Fe²⁺ co-doped ZnO with the addition of HSO₅⁻: Toxicities and degradation pathways investigation, *Chem. Eng. J.* 351 (2018) 841–855.
- [25] P. Hu, M. Long, Cobalt-catalyzed sulfate radical-based advanced oxidation: A review on heterogeneous catalysts and applications, *Appl. Catal. B Environ.* 181 (2016) 103–117.
- [26] K.A. Lin, H. Chang, Zeolitic Imidazole Framework-67 (ZIF-67) as a heterogeneous catalyst to activate peroxymonosulfate for degradation of Rhodamine B in water, *J. Taiwan Inst. Chem. E.* 53 (2015) 40–45.
- [27] A. Al-Anazi, W.H. Abdelraheem, C. Han, M.N. Nadagouda, L. Sygellou, M.K. Arfanis, P. Falaras, V.K. Sharma, D.D. Dionysiou, Cobalt ferrite nanoparticles with controlled composition-peroxymonosulfate mediated degradation of 2-phenylbenzimidazole-5-sulfonic acid, *Appl. Catal. B Environ.* 221 (2018) 266–279.
- [28] J. Li, M. Xu, G. Yao, B. Lai, Enhancement of the degradation of atrazine through CoFe₂O₄ activated peroxymonosulfate (PMS) process: Kinetic, degradation intermediates, and toxicity evaluation, *Chem. Eng. J.* 348 (2018) 1012–1024.
- [29] S. Yang, X. Qiu, P. Jin, M. Dzakpasu, X.C. Wang, Q. Zhang, L. Zhang, L. Yang, D. Ding, W. Wang, K. Wu, MOF-templated synthesis of CoFe₂O₄ nanocrystals and its coupling with peroxymonosulfate for degradation of bisphenol a, *Chem. Eng. J.* 353 (2018) 329–339.
- [30] K. Zhang, D. Sun, C. Ma, G. Wang, X. Dong, X. Zhang, Activation of peroxymonosulfate by CoFe₂O₄ loaded on metal-organic framework for the degradation of organic dye, *Chemosphere* 241 (2020) 125021.
- [31] Y. Li, X. Yan, X. Hu, R. Feng, M. Zhou, Trace pyrolyzed ZIF-67 loaded activated carbon pellets for enhanced adsorption and catalytic degradation of Rhodamine B in water, *Chem. Eng. J.* 375 (2019) 122003.
- [32] L. Yang, M.A. Carreon, Deoxygenation of palmitic and lauric acids over Pt/ZIF-67 Membrane/Zeolite 5A bead catalysts, *ACS Appl. Mater. Inter.* 9 (2017) 31993–32000.
- [33] L. Peng, X. Gong, X. Wang, Z. Yang, Y. Liu, In situ growth of ZIF-67 on a nickel foam as a three-dimensional heterogeneous catalyst for peroxymonosulfate activation, *RSC Adv.* 8 (2018) 26377–26382.
- [34] C. Wu, W. Yun, T. Wi-Afedzi, K.A. Lin, ZIF-67 supported on macroscale resin as an efficient and convenient heterogeneous catalyst for Oxone activation, *J. Colloid Interf. Sci.* 514 (2018) 262–271.
- [35] N. Li, G. Chen, J. Zhao, B. Yan, Z. Cheng, L. Meng, V. Chen, Self-cleaning PDA/ZIF-67@PP membrane for dye wastewater remediation with peroxymonosulfate and visible light activation, *J. Membr. Sci.* 591 (2019) 117341.
- [36] Y. Jo, T. Kim, C. Lee, K. Lim, C.W. Na, F. Abdel-Hady, A.A. Wazzan, J. Lee, Metal-organic Framework-Derived hollow hierarchical Co₃O₄ nanocages with tunable size and morphology: Ultrasensitive and highly selective detection of methylbenzenes, *ACS Appl. Mater. Inter.* 10 (2018) 8860–8868.
- [37] Y. Bao, W. Oh, T. Lim, R. Wang, R.D. Webster, X. Hu, Surface-nucleated heterogeneous growth of zeolitic imidazolate framework – a unique precursor towards catalytic ceramic membranes: Synthesis, characterization and organics degradation, *Chem. Eng. J.* 353 (2018) 69–79.
- [38] J.E. Yang, Y. Lin, H. Peng, B. Yuan, D.D. Dionysiou, X. Huang, D. Zhang, M. Fu, Novel magnetic rod-like Mn-Fe oxycarbide toward peroxymonosulfate activation for efficient oxidation of butyl paraben: Radical oxidation versus singlet oxygenation, *Appl. Catal. B Environ.* 268 (2020) 118549.
- [39] J. Huo, L. Xu, X. Chen, Y. Zhang, J.E. Yang, B. Yuan, M. Fu, Direct epitaxial synthesis of magnetic Fe₃O₄@UiO-66 composite for efficient removal of arsenate from water, *Micropor. Mesopor. Mat.* 276 (2019) 68–75.
- [40] J. Huo, K. Gupta, C. Lu, H.C. Bruun Hansen, M. Fu, Recyclable high-affinity arsenate sorbents based on porous Fe₂O₃/La₂O₂CO₃ composites derived from Fe-La-C frameworks, *Colloid. Surface. A* 585 (2020) 124018.
- [41] L. Rizzo, C. Manaia, C. Merlin, T. Schwartz, C. Dagot, M.C. Ploy, I. Michael, D. Patta-Kassinou, Urban wastewater treatment plants as hotspots for antibiotic resistant bacteria and genes spread into the environment: A review, *Sci. Total Environ.* 447 (2013) 345–360.
- [42] C. Liang, C. Huang, N. Mohanty, R.M. Kurakalva, A rapid spectrophotometric determination of persulfate anion in ISCO, *Chemosphere* 73 (2008) 1540–1543.
- [43] Y. Zhang, J.E. Yang, M. Fu, B. Yuan, K. Gupta, One-step fabrication of recycled Ag nanoparticles/graphene aerogel with high mechanical property for disinfection and catalytic reduction of 4-nitrophenol, *Environ. Technol.* 40 (2018) 3381–3391.
- [44] J. Qin, S. Wang, X. Wang, Visible-light reduction CO₂ with dodecahedral zeolitic imidazolate framework ZIF-67 as an efficient co-catalyst, *Appl. Catal. B Environ.* 209 (2017) 476–482.
- [45] R. Ma, Z. Liu, K. Takada, K. Fukuda, Y. Ebina, Y. Bando, T. Sasaki, Tetrahedral Co (II) coordination in α-Type cobalt hydroxide: Rietveld refinement and x-ray absorption spectroscopy, *Inorg. Chem.* 45 (2006) 3964–3969.
- [46] W. Zheng, M. Liu, L.Y.S. Lee, Electrochemical instability of metal-organic frameworks: In situ spectroelectrochemical investigation of the real active sites, *ACS Catal.* 10 (2019) 81–92.
- [47] L. Liotta, CoO_x catalysts supported on alumina and alumina-baria: Influence of the support on the cobalt species and their activity in NO reduction by C₃H₆ in lean conditions, *Appl. Catal. A: General* 245 (2003) 167–177.
- [48] S. Kurajica, J. Popović, E. Tkalčec, B. Gržeta, V. Mandić, The effect of annealing temperature on the structure and optical properties of sol-gel derived nanocrystalline cobalt aluminate spinel, *Mater. Chem. Phys.* 135 (2012) 587–593.
- [49] L. Vndewater, G. Bezemer, J. Bergwerff, M. Versluisshelder, B. Weckhuysen, K. Dejong, Spatially resolved UV-vis microspectroscopy on the preparation of alumina-supported Co Fischer-Tropsch catalysts: Linking activity to Co distribution and speciation, *J. Catal.* 242 (2006) 287–298.
- [50] S. Velu, K. Suzuki, S. Hashimoto, N. Satoh, F. Ohashi, S. Tomura, The effect of cobalt on the structural properties and reducibility of CuCoZnAl layered double hydroxides and their thermally derived mixed oxides, *J. Mater. Chem.* 112049-2060.
- [51] S. Morpurgo, M. Lo Jacono, P. Porta, Pillared hydroxycarbonates and mixed oxides. Part 1. —Copper-zinc-cobalt-aluminium system, *J. Mater. Chem.* 4 (1994) 197–204.
- [52] Y. Tang, C. Wu, Y. Song, Y. Zheng, K. Zhao, Effects of colouration mechanism and stability of CoAl₂O₄ ceramic pigments sintered on substrates, *Ceram. Int* 44 (2018) 1019–1025.
- [53] M. Zhang, Q. Dai, H. Zheng, M. Chen, L. Dai, Novel MOF-derived Co@N-C bifunctional catalysts for highly efficient Zn-Air batteries and water splitting, *Adv. Mater.* 30 (2018) 1705431.
- [54] Z. Liu, H. Tan, D. Liu, X. Liu, J. Xin, J. Xie, M. Zhao, L. Song, L. Dai, H. Liu, Promotion of overall water splitting activity over a wide pH range by interfacial electrical effects of metallic NiCo-nitrides Nanoparticle/NiCo₂O₄ nanoflake/graphite fibers, *Adv. Sci.* 6 (2019) 1801829.
- [55] J. Yang, H. Liu, W.N. Martens, R.L. Frost, Synthesis and characterization of cobalt hydroxide, cobalt oxyhydroxide, and cobalt oxide nanodisks, *J. Phys. Chem. C* 114 (2009) 111–119.
- [56] G. Li, L. Li, J. Shi, Y. Yuan, Y. Li, W. Zhao, J. Shi, One-pot pyrolytic synthesis of mesoporous MCo₂O₄(4.5) (M=Mn, Ni, Fe, Cu) spinels and its high efficient catalytic properties for CO oxidation at low temperature, *J. Mol. Catal. A Chem.* 390 (2014) 97–104.
- [57] X. Duan, M. Pan, F. Yu, D. Yuan, Synthesis, structure and optical properties of CoAl₂O₄ spinel nanocrystals, *J. Alloy Compd.* 509 (2011) 1079–1083.
- [58] L. Zhuang, L. Ge, Y. Yang, M. Li, Y. Jia, X. Yao, Z. Zhu, Ultrathin Iron-Cobalt oxide nanosheets with abundant oxygen vacancies for the oxygen evolution reaction, *Adv. Mater.* 29 (2017) 1606793.
- [59] J.E. Yang, H. Lan, X. Lin, B. Yuan, M. Fu, Synthetic conditions-regulated catalytic Oxone efficacy of MnO_x/SBA-15 towards butyl paraben (BPB) removal under heterogeneous conditions, *Chem. Eng. J.* 289 (2016) 296–305.
- [60] J. Yan, L. Han, W. Gao, S. Xue, M. Chen, Biochar supported nanoscale zerovalent iron composite used as persulfate activator for removing trichloroethylene, *Bioresour. Technol.* 175 (2015) 269–274.
- [61] Y. Guan, J. Ma, X. Li, J. Fang, L. Chen, Influence of pH on the formation of sulfate and hydroxyl radicals in the UV/Peroxymonosulfate system, *Environ. Sci. Technol.*

- 45 (2011) 9308–9314.
- [62] C.F. Rediguieri, V. Porta, D.S.G. Nunes, T.M. Nunes, H.E. Junginger, S. Kopp, K.K. Midha, V.P. Shah, S. Stavchansky, J.B. Dressman, D.M. Barends, Biowaiver monographs for immediate release solid oral dosage forms: Metronidazole, *J. Pharm. Sci-US* 100 (2011) 1618–1627.
- [63] X. Lou, L. Wu, Y. Guo, C. Chen, Z. Wang, D. Xiao, C. Fang, J. Liu, J. Zhao, S. Lu, Peroxymonosulfate activation by phosphate anion for organics degradation in water, *Chemosphere* 117 (2014) 582–585.
- [64] J.E. Yang, B. Yuan, H. Cui, S. Wang, M. Fu, Modulating oxone-MnO_x/silica catalytic systems towards ibuprofen degradation: Insights into system effects, reaction kinetics and mechanisms, *Appl. Catal. B Environ.* 205 (2017) 327–339.
- [65] Y. Bao, T. Lim, R. Wang, R.D. Webster, X. Hu, Urea-assisted one-step synthesis of cobalt ferrite impregnated ceramic membrane for sulfamethoxazole degradation via peroxymonosulfate activation, *Chem. Eng. J.* 343 (2018) 737–747.
- [66] T.N. Das, R.E. Huie, P. Neta, Reduction Potentials of SO₃^{•-}, SO₅^{•-}, and S₄O₆^{•3-} Radicals in Aqueous Solution, *J. Phys. Chem. A* 103 (1999) 3581–3588.
- [67] J. Lee, U. von Gunten, J. Kim, Persulfate-Based advanced oxidation: Critical assessment of opportunities and roadblocks, *Environ. Sci. Technol.* 54 (2020) 3064–3081.
- [68] Y. Zheng, Y. Liu, H. Zhou, W. Huang, Z. Pu, Complete combustion of methane over Co₃O₄ catalysts: Influence of pH values, *J. Alloy Compd.* 734 (2018) 112–120.
- [69] W. Ren, L. Xiong, X. Yuan, Z. Yu, H. Zhang, X. Duan, S. Wang, Activation of peroxydisulfate on carbon nanotubes: Electron-transfer mechanism, *Environ. Sci. Technol.* 53 (2019) 14595–14603.
- [70] E. Yun, J.H. Lee, J. Kim, H. Park, J. Lee, Identifying the nonradical mechanism in the peroxymonosulfate activation process: Singlet oxygenation versus mediated electron transfer, *Environ. Sci. Technol.* 52 (2018) 7032–7042.
- [71] J. Yoon, S.W. Kang, W. Shim, J.K. Lee, D.K. Jang, N. Gu, S.K. Kim, K. Lee, E.K. Chung, Quantification of metronidazole in human bile fluid and plasma by liquid chromatography-tandem mass spectrometry, *J. Chromatogr. B* 1138 (2020) 121959.
- [72] R.H.M.M. Granja, A.M.M. Nino, K.V.G. Reche, F.M. Giannotti, A.C. de Lima, A.C.B.A. Wanschel, A.G. Salerno, Determination and confirmation of metronidazole, dimetridazole, ronidazole and their metabolites in bovine muscle by LC-MS/MS, *Food Addit. Contam. A* 30 (2013) 970–976.
- [73] X. Zhu, Y. Wang, C. Liu, W. Qin, D. Zhou, Kinetics, intermediates and acute toxicity of arsanilic acid photolysis, *Chemosphere* 107 (2014) 274–281.